Diagnosing Warm Frontal Cloud Formation in a GCM: A Novel Approach Using Conditional Subsetting

JAMES F. BOOTH

NASA Goddard Institute for Space Studies, and Applied Physics and Applied Mathematics, Columbia University, New York, New York

CATHERINE M. NAUD

Applied Physics and Applied Mathematics, Columbia University, New York, New York

ANTHONY D. DEL GENIO

NASA Goddard Institute for Space Studies, New York, New York

ABSTRACT

This study analyzes characteristics of clouds and vertical motion across extratropical cyclone warm fronts in the NASA Goddard Institute for Space Studies general circulation model. The validity of the modeled clouds is assessed using a combination of satellite observations from *CloudSat, Cloud–Aerosol Lidar and Infrared Pathfinder Satellite Observations* (*CALIPSO*), Advanced Microwave Scanning Radiometer for Earth Observing System (AMSR-E), and the NASA Modern-Era Retrospective Analysis for Research and Applications (MERRA) reanalysis. The analysis focuses on developing cyclones, to test the model's ability to generate their initial structure. To begin, the extratropical cyclones and their warm fronts are objectively identified and cyclone-local fields are mapped into a vertical transect centered on the surface warm front. To further isolate specific physics, the cyclones are separated using conditional subsetting based on additional cyclone-local variables, and the differences between the subset means are analyzed. Conditional subsets are created based on 1) the transect clouds and 2) vertical motion; 3) the strength of the temperature gradient along the warm front, as well as the storm-local 4) wind speed and 5) precipitable water (PW). The analysis shows that the model does not generate enough frontal cloud, especially at low altitude. The subsetting results reveal that, compared to the observations, the model exhibits a decoupling between cloud formation at high and low altitudes across warm fronts and a weak sensitivity to moisture. These issues are caused in part by the parameterized convection and assumptions in the stratiform cloud scheme that are valid in the subtropics. On the other hand, the model generates proper covariability of low-altitude vertical motion and cloud at the warm front and a joint dependence of cloudiness on wind and PW.

1. Introduction

Extratropical cyclones play a dominant role in midlatitude circulation, affecting both weather and climate. These storms are driven primarily by dry dynamics (e.g., Holton 1992, 229–230); however, the moist processes and their products within the storms are also important. For example, the fronts of extratropical cyclones are the source of the majority of midlatitude precipitation in winter, especially over the ocean (Catto et al. 2012). Also, moisture can affect storm strength through condensational heating, which can generate stronger surface winds (Stoelinga 1996). Accumulated over longer time scales, the moist circulation in cyclones has a unique role in the earth's radiation budget because the optically thick clouds associated with cyclones have a significant radiative impact in the midlatitudes during winter (Tselioudis et al. 2000; Haynes et al. 2011).

Unfortunately, general circulation models (GCMs) have difficulty capturing some aspects of the moist processes in midlatitudes. For instance, the observed storm precipitation rates and their spatial patterns are not

Corresponding author address: James F. Booth, NASA GISS, 2880 Broadway, New York, NY 10025.
E-mail: jbooth.atmos@gmail.com

reproduced in model hindcasts (Stephens et al. 2010). Additionally, model cloud errors produce biases in the radiation budget in the midlatitudes (Trenberth and Fasullo 2010). This specific issue may be predominantly related to low-level clouds, which are more prevalent (Haynes et al. 2011). However, the clouds within extratropical cyclones are also biased in the models. For instance, Field et al. (2008) found that the National Center for Atmospheric Research Community Atmosphere Model, version 3 (CAM3), overestimated the cyclone-centered high-topped clouds and rain rates compared to observations. In the National Aeronautics and Space Administration (NASA) Goddard Institute for Space Studies (GISS) GCM, Naud et al. (2010) found that frontal cloud fraction was too small compared to observations at all altitudes, most likely due to the vertical motion in the model being too weak. For the Hadley Centre GCM, Catto et al. (2010) found that the vertical motion within cyclones matched that of reanalysis, but the model relative humidity (RH) was too low, especially at mid and high altitudes. Biases in extratropical cyclone cloudiness also occurred in a previous version of the Met Office Unified Model (Field et al. 2011; Bodas-Salcedo et al. 2012).

The need to properly model the moist processes within extratropical cyclones is made more important by the projected increase in atmospheric moisture content that will accompany global warming (e.g., Held and Soden 2006). The increase in moisture could lead to more condensation within the storms, and/or increasing cyclone cloudiness could act as a feedback on the surface temperature (Tselioudis and Rossow 2006). However, cloud formation within cyclones in GCMs depends on complex interactions between the large-scale circulation and local parameterizations that have not been evaluated sufficiently. These issues, as well as GCM biases in the midlatitude radiation budget (Trenberth and Fasullo 2010), motivate the following questions: Are midlatitude cloud biases in GCMs occurring within the modeled extratropical cyclones? If so, at what horizontal and vertical locations are the biases occurring within the storm? Furthermore, are the biases caused by resolved or parameterized physics in the models?

To address these questions, this paper evaluates extratropical cyclones' cloud distributions in the NASA GISS ModelE2 GCM (G. Schmidt et al. 2013, unpublished manuscript) using cyclone compositing. Compositing was used in some of the cloud studies referred to above (Field et al. 2008; Naud et al. 2010; Catto et al. 2010; Field et al. 2011) and has been helpful for understanding other aspects of cyclones characteristics as well (e.g., Lau and Crane 1995; Bauer and Del Genio 2006; Naud et al. 2006; Chang and Song 2006; Bengtsson et al. 2009; Rudeva and Gulev 2011).

Here we use cyclone compositing to isolate the warm frontal clouds within the extratropical cyclones from other cloud systems that would be present in any Eulerian analysis, such as the semipermanent cloud features in the midlatitudes or isolated convective systems. Furthermore, to assess the vertical location of GCM biases, we compare model output with vertical transects from *CloudSat* radar (Stephens et al. 2002) and *Cloud–Aerosol Lidar and Infrared Pathfinder Satellite Observations* (*CALIPSO*) lidar (Winker et al. 2009) observations. Given the different radiative impacts of high and low-altitude clouds, assessing the vertical structure is important for understanding the GCM's radiation biases.

We extend the utility of compositing by conditionally subsetting the cyclone composites using other characteristics of the cyclones. This allows us to assess both the covariability of the clouds and vertical motion, as well as their relationships with other dynamic and thermodynamic properties of the cyclones. This subsetting technique has been used previously with success. For one, Field and Wood (2007, hereafter FW07) showed that cyclone high-topped clouds and precipitation had a joint dependence on precipitable water (PW) and wind speed. In addition, Naud et al. (2012) found differences in cloud evolution within storm life cycles for the Northern versus Southern Hemisphere related to differences in the storm cloud's relative dependence on wind speed and PW. Expanding on those results, we show that the composite mean cloud fields and the covariability of the cloud fields with other variables can give complementary information, somewhat analogous to the tropical vertical-velocity-based separation technique of Bony et al. (2004).

2. Data and methods

This paper compares warm frontal clouds in extratropical cyclones in the GISS ModelE2 with observations from a *CloudSat–CALIPSO* satellite product, using the four November–March periods between 2006 and 2010. We choose the warm front because it is the part of the cyclone that has the largest cloud cover. We focus on cyclones in the Northern Hemisphere, because Naud et al. (2012) found differences in cyclone cloud development between the two hemispheres. To avoid temperature contrast issues at coastlines or topography, we only study cyclones over the ocean.

a. Observations and reanalysis

For cloud observations across the warm fronts, we use vertical profiles of hydrometeor location from the combined product Geometrical Profiling Product (GEOPROF) lidar (Mace et al. 2009) retrieved with both *CloudSat* radar (Stephens et al. 2002) and *CALIPSO* lidar (Winker

et al. 2009) observations. These hydrometeors can be either suspended droplets, ice crystals, or precipitation, but for simplicity we call them cloud. Each GEOPROF lidar profile is transformed from a series of cloud base and top altitudes into a common 250-m resolution vertical grid where a cloud mask indicates the presence or absence of hydrometeors. Near the surface, cloud detection with *CloudSat* is hindered by the strong surface signal (Marchand et al. 2008); therefore, we omit data below 1.2 km from our analysis.

For precipitable water observations, we use the Advanced Microwave Scanning Radiometer for Earth Observing System (AMSR-E) (Kawanishi et al. 2003) retrievals (Wentz and Meissner 2004) coincident with the *CloudSat–CALIPSO* observations. AMSR-E retrievals are only available over the open ocean, so there are fewer data points to the east of the ocean basins and poleward of the fronts.

For all other cyclone variables that we compare with the model, we use the NASA Modern-Era Retrospective Analysis for Research and Applications (MERRA) (Rienecker et al. 2011). These variables are 850-hPa wind speed and potential temperature (θ); vertical velocity using pressure as the vertical coordinate (ω); sea level pressure (SLP); and 300-hPa absolute vorticity advection, which is calculated from MERRA winds. For the identification of warm fronts collocated with the *CloudSat* orbits (see section 2c for details on front detection), we use MERRA 850-hPa θ and geopotential height because it is available at a fine horizontal resolution ($0.5° \times 0.667°$). This allows a more precise intersect with the satellite orbits.

b. The model

For the model analysis, we run the atmosphere component of GISS ModelE2 using the standard configuration used for the World Climate Research Programme's phase 5 of the Coupled Model Intercomparison Project (CMIP5). This configuration entails horizontal grid spacing of 2° latitude by 2.5° longitude and 40 vertical levels. For details on the model's mean state and the physics of its parameterization schemes, see G. Schmidt et al. (2013, unpublished manuscript) and references therein. Here, we briefly describe the GCM approach to forming clouds. Stratiform cloud fraction is a diagnostic function of relative humidity with a threshold humidity value below which stratiform clouds do not form (Del Genio et al. 1996). Cloud areal fraction equals cloud volume fraction in unstable environments but exceeds volume fraction in stable environments; that is, a model layer is not always filled vertically with cloud for the calculation of cloud fraction and optical thickness. The reference for calculating relative humidity is water

saturation for temperature above $-35°C$ and the critical humidity for homogeneous freezing given by Kärcher and Lohmann (2002) at colder temperatures. Stratiform clouds do not form in subsaturated air below cloud top in the convective portion of a grid box or below the cloud base of a boundary-layer convective cloud.

Naud et al. (2010) found limitations in the cloud scheme in the previous version of the GCM such that clouds formed at higher relative humidity than combined observations and reanalysis suggested. This motivated a change in the cloud scheme for the present model version to allow the relative humidity threshold for cloud formation to vary with environmental state: for boundary layer clouds (pressure > 850 hPa) the threshold is based on an assumed Gaussian distribution of saturation deficit as given by Siebesma et al. (2003), while in the free troposphere the threshold decreases in the presence of strong gridscale rising motion to mimic the effect of unresolved frontal uplift, with a scale-aware correction for varying layer thickness. The GCM also calculates a convective cloud fraction based on the cumulus mass flux and convective updraft speed, but this usually contributes <10% to the total cloud fraction in the extratropics.

The boundary conditions and forcing of the model are as follows. The greenhouse gas concentrations are fixed at 1979 levels to match Naud et al. (2010). The ozone and aerosol concentrations are prescribed inputs based on observational datasets. This is the same configuration used in the noninteractive chemistry (NINT) runs submitted by GISS to CMIP5. The prescribed sea surface temperatures (SSTs), which evolve in time, are based on the monthly Hadley Centre Sea Ice and Sea Surface Temperature dataset, version 1 (HadISST1) (Rayner et al. 1996).

For our analysis we use three years of model output that correspond to SSTs for 1990–92. However, because the greenhouse gas forcing is fixed, these dates are somewhat arbitrary. The use of three winters of data provides a larger sample size and removes any potential biases related to interannual variability in the geographical locations of cyclone paths.

c. Cyclone tracking and warm front identification

The preliminary steps taken to identify candidate cyclones follow that of Naud et al. (2010). Here we list them briefly and then discuss each in detail (see also Fig. 1).

1) Cyclones are identified every 6 h using a SLP tracking algorithm.
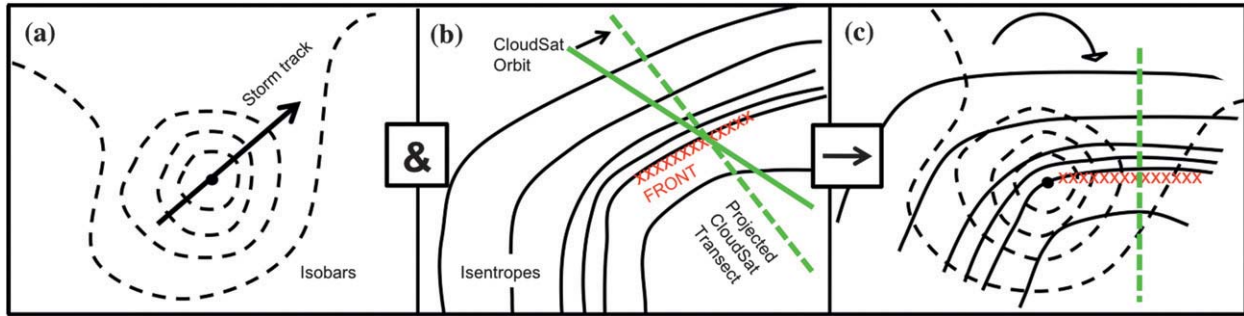2) Separately, warm fronts are identified using θ at 850 hPa.

FIG. 1. Steps for producing the cyclone composites: (a) storm identification, dashed lines represent idealized SLP contours and the arrow (dot) indicates storm track(center), identified by MCMS algorithm; (b) warm front identification and transect projection, solid black lines represent idealized $\theta_{850\,hPa}$ contours for same time and location as in the left panel, red crosses represent the warm front identified by the Hewson (1998) algorithm, the solid green line indicates the location of near-coincident *CloudSat* orbit, and the dashed green line the projection of *CloudSat* profiles onto perpendicular to front (arrow indicates direction of the projection); and (c) rotation to warm front coordinate system in which SLP and $\theta_{850\,hPa}$ from (a),(b) have been rotated so that the warm front is on the horizontal axis at center of the grid and the arrow at the top shows the direction of rotation.

3) Cyclones for which warm fronts are detected are selected for further analysis.

To identify the cyclones (e.g., Fig. 1a) we use the algorithm in Bauer et al. (2012, manuscript submitted to *J. Appl. Meteor. Climatol.*), which is an update of the algorithm in Bauer and Del Genio (2006). For the observations and reanalysis, the cyclones are identified using the Modeling, Analysis and Prediction (MAP) Climatology of Midlatitude Storminess (MCMS), a database of cyclone tracks created using SLP from the European Centre for Medium-Range Weather Forecasts Interim Re-Analysis (ERA-Interim) (Simmons et al. 2007), which captures extratropical cyclone tracks as well as any other reanalysis product (Hodges et al. 2011). For the model, we run the same MCMS tracking algorithm on the model SLP output.

The MCMS tracking algorithm is one of many automated schemes available (e.g., Neu et al. 2013), and with each scheme there are biases. However, as discussed in Neu et al. (2013), the biases are smaller for cyclones that occur over the ocean, particularly those that are long lived and travel far, which are the storms that we focus on in this analysis. There could be a separate bias associated with the resolution of the SLP grid, which is finer for reanalysis compared to the model. This may allow the tracker to identify the reanalysis cyclones slightly earlier in their development.

In addition to the cyclone tracking, we track warm fronts by applying the front detection algorithm of Hewson (1998) to θ at 850 hPa (i.e., Fig. 1b; see also Naud et al. 2010, Fig. 1). The Hewson (1998) method determines frontal locations using threshold values for the strength of the temperature gradient and the spatial rate of change of the strength of the gradient $\nabla(|\nabla\theta|)$.

Then, in the regions that pass the threshold test, the divergence of $\mathbf{V}(|\nabla\theta|)$ is calculated in an "along-gradient divergence" coordinate system. The fronts are identified as the locations at which the along-gradient divergence is equal to zero [for explanations on the thresholds that we use, see Naud et al. (2010), section 3b]. Additionally, Naud et al. visually tested the validity of the tracker for one winter.

We associate a warm front with a cyclone if 1) the center of the warm front is within 1500 km of the low, 2) the warm front is to the east of the low, and 3) the distance between the warm front center and the low is less than 5° in latitude. If more than one candidate warm front meets these criteria, then we use the warm front that exhibits the greatest temperature gradient. By associating the fronts with cyclones, we guarantee that our study focuses on mobile fronts.

We use the term "storm event" to refer to the complete baroclinic life cycle, from genesis to lysis, and "cyclone" to refer to individual snapshots of the storms, consistent with the terminology used in Naud et al. (2010, 2012), Pinto et al. (2009), and Catto et al. (2010). To ensure that we are studying canonical extratropical cyclones, we only use cyclones in storm events with at least a 36-h lifespan that travel greater than 3000 km. We focus on the cyclones found within a fixed latitude band (30°–60°N) that occur during onset, defined as the period from first detection until the midpoint between the first detection time and the time of the storm's maximum strength (minimum SLP). The reasons we study storms at onset are 1), if there are initial errors in the modeled cyclones, they will most likely affect the entire life span of the storm and 2) it becomes complicated to pinpoint the causes for discrepancies between the modeled cyclones and reality
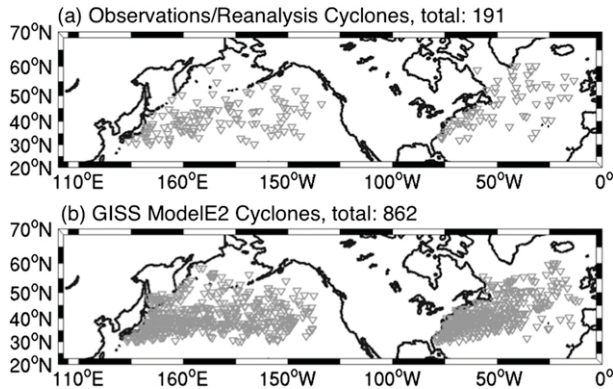
FIG. 2. Geographical location of the cyclones studied here for (a) the observations and reanalysis dataset and (b) the model.

later in the storm life cycle because the storms become more complex.

As a final step, we generate a subset of the modeled cyclones by randomly drawing from the whole set so that the latitudinal distribution of the subset matches that of the observed cyclones. This ensures more similar distributions of moisture and sea surface temperature in the cyclone-centered variables. We also confirmed that the longitude distributions are similar for the two cyclone sets. The final datasets contain 191 observed and 862 modeled cyclones (the model set being larger because of its complete space–time sampling). Figure 2 shows the geographical locations for the cyclones in the two sets.

d. Compositing

After the candidate cyclones are identified with warm fronts, we map atmospheric variables in two orientations relative to the cyclones: 1) a vertical transect perpendicular to the warm front and 2) a cyclone-centered view.

For the cyclone-transect variables, we fit a straight line through the low and the warm front grid points to obtain the overall orientation of the warm front. Then, for each point along the front we collect information along the perpendicular to this fit within ±10° of the front (Fig. 1b). This methodology will cause some displacement of the perpendicular with respect to its real position. However, this displacement is random and, after compositing multiple transects together, is expected to have a negligible impact.

For the cloud observations we use the same technique as in Naud et al. (2010) to collect and visualize the data. When the *CloudSat* orbit intersects a warm front within ±3 h, the cloud mask profiles are collected in a grid of 0.2° horizontal resolution and 250-m vertical resolution. To do this, we take the perpendicular to the front

positioned at the intersect and project the observed profiles onto that perpendicular (Fig. 1b). In each $0.2° \times 250$ m grid box we then calculate the ratio of number of cloud detections to the total number of profiles per column. The result is then the frequency of cloud occurrence, which, again for simplicity, we refer to as cloud fraction. Because *CloudSat–CALIPSO* composites include precipitating particles, the observed cloud fraction is overestimated by ~10%, according to Naud et al. (2010). Nearly coincident ω, RH, and temperature transects for each retained *CloudSat* orbit intersect are obtained from MERRA.

For the model, we average together a set of transects perpendicular to the front. Given the coarse resolution of the model, this approach captures the cloud features over the region in a manner that is most consistent with our treatment of the *CloudSat* orbit. Because MERRA has finer resolution, we used it to compare the two techniques. We find that the averaging technique used on the model only slightly increases the cloud content in the transect (not shown). The cyclone-transect variables that we consider for the model are total cloud fraction, pressure vertical velocity ω, relative humidity (RH), as well as the model's threshold RH (RH00), and convective heating.

For the cyclone-centered view, we analyze variables within a 2500-km radius around the cyclone center. These fields are projected onto a stereographic grid and rotated (Fig. 1c) so that the warm fronts for each cyclone are aligned along the west–east horizontal axis to the east of the cyclone center as in Naud et al. (2012). The cyclone-centered variables that we compare between MERRA and the model are SLP, wind speed, and θ at 850 hPa, ω at 500 hPa, and the vertical component of absolute vorticity advection at 300 hPa. We also compare the model PW with that of AMSR-E.

Our method of projecting the data onto a stereographic grid with equal length radii removes the biases associated with the convergence of the meridians. However, there are other normalization techniques, such as that of Rudeva and Gulev (2011) or Catto et al. (2010). In our case, the key step is our rotation of the cyclone-centered fields to align the warm fronts. This guarantees that in our region of interest, the warm front, the cyclone characteristics being averaged together are consistent. On the other hand, with any compositing analysis, the averaging and the projecting introduces some biases, so we focus here on the differences between the model and observations.

e. Conditional subset differencing

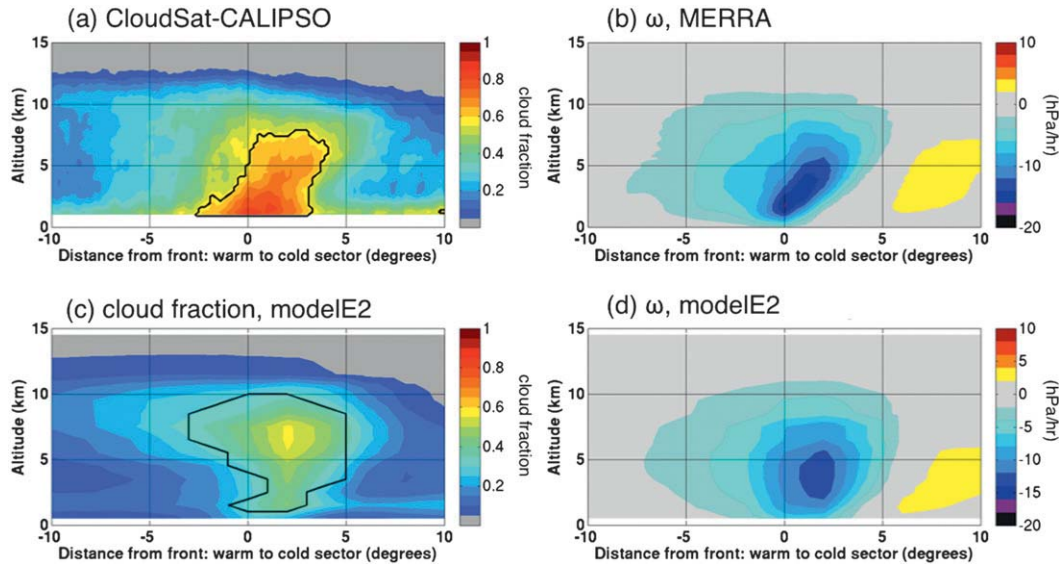The conditional subsetting method consists of three steps:

FIG. 3. Composite mean of cloud fraction and ω transects perpendicular to the warm front: (a) *CloudSat–CALIPSO* cloud fraction, (b) MERRA ω, and ModelE2 (c) cloud fraction and (d) ω (hPa h^{-1}). In (a),(c) the black contour shows the top 85th percentile (0.58 for the data, 0.31 for the model) used to define the subsetting area.

1) Area average a cyclone-centered or cyclone-transect variable over the subdomain of interest (in our case, in the vicinity of the warm front).
2) Divide the distribution of area averages for all cyclones into "strong" and "weak" subsets with area averages greater and less than the mean area average for all cyclones, respectively.
3) Calculate the cyclone mean for both subsets and difference them: strong − weak.

Determining the region used for calculating the area average is subjective. Sensitivity of the results to the area-averaging region is discussed in the appendix.

For the subset results, we only show the differences that are statistically significant at the 95% significance level. For any location in our cyclone-specific fields, it is not obvious that the distributions across the cyclones are normally distributed. Therefore, we compared results for three types of significance testing: 1) the standard Student's t test, 2) the Whitney–Mann—or Wilcoxon rank sum—test, and 3) a boot-strap approach in which subsets of random cyclones are differenced to create a distribution of differences to compare against the subset differences. For each case the results were similar; however, a fewer points are found to be significant by the Student's t test as compared to the other two tests, so we show results based on it.

3. Composite means and conditional subsets

We first compare the composite means using all cyclones for the observations/reanalysis versus ModelE2

and then move on to the conditional subsetting. To complement our compositing analysis, we also compare the geographical locations, maximum strength, and duration of extratropical storm events from the model with those from ERA-Interim. For these metrics, the model matches the reanalysis except for the extremely strong storms (not shown). One glaring difference however is that the modeled storm intensification rates are weaker than those in the reanalysis. This result may primarily be due to lower resolution of the GISS GCM relative to the weather prediction models used to create the reanalysis but may be partially caused by too weak condensational forcing in the cyclone warm sector (Booth et al. 2013).

a. Subsets based on cyclone-transect variables

Figures 3a and 3b show transects of the composite mean cloud fraction from *CloudSat–CALIPSO* and ω from MERRA. Cloud fraction peaks at the surface front and tilts poleward with height. There is a secondary maximum in low-level (1–2 km) cloudiness on either side of the surface front. The standard deviation of cloud fraction across all cyclones, at each latitude/pressure in the transect, has a local minimum (not shown) in the region where the composite average has a local maximum. This suggests that the patterns are robust to the errors inherent in compositing. The spatial distribution of ω is consistent with the cloud fraction: the region of strong upward motion tilts poleward with height and has a sharp gradient on the poleward edge of the frontal tilt region. These results for cyclones at onset agree with those of Naud et al. (2010) for the entire life cycle.

Figure 3c shows the modeled cyclone composite mean cloud fraction. As in the observations, the region of highest cloud fraction tilts poleward with height, and there is also a local peak in low cloud fraction ahead of the front. However, the model cloud fraction is too small below 10 km, especially below 5 km (e.g., observed cloud fraction is 0.8, versus 0.4 for the model). These differences are larger than the ~10% high bias in satellite data, a conclusion also reached by Naud et al. (2010).

Related to the cloud issue, comparing Figs. 3b and 3d shows that ω at the transect is too weak in the model: along the front, the model's strongest ω is $-12\,\mathrm{hPa\,h}^{-1}$ versus $-16\,\mathrm{hPa\,h}^{-1}$ for MERRA. The model ω differs from MERRA in three other ways: 1) the front is too upright, 2) the strongest frontal ω values do not extend down to the surface, and 3) the strongest upward motion is at a lower altitude than the peak cloud fraction. Part of the weak tilt with height can be attributed to the model's coarse resolution, which does not resolve frontogenesis processes that are responsible for most frontal cloudiness. However, the subsetting analysis below reveals that model physics also plays a role.

To illustrate the subsetting approach, we first consider an intuitive example: cloud-based subsetting applied to the cloud and ω fields. To define the area-averaging region, we rank the values from all points in the composite mean transect and enclose the top 85th percentile. Thus, the averaging region differs in the observations and the model (see black contours in Figs. 3a,c). We choose an area defined relative to the composite mean, rather than a fixed location, because the regions of maximum clouds in the observations and model differ, so using a fixed region would not isolate the strongest cloud cases from both datasets. The 85th percentile threshold is chosen because it includes the largest amount of the frontal clouds without capturing the low-altitude cloud poleward of the frontal region.

Figure 4 shows the distributions of the area-averaged cloud fractions for the observations and model. The observations have more cloud and the distribution is skewed toward low values, while the model is nearly symmetric about the mean. The means for the distributions are used to mark the separation between the strong and weak subsets for the cloud-based subsetting that follows. For both observations and model there is no difference in month of year or the geographical locations of the cyclones in the strong- and weak-cloud subsets (not shown).

Figure 5 shows the results of the cloud-based subsetting applied to the cloud and ω transects. In each panel, the color shading shows the subset differences, and black contours show the composite mean using all cyclones. Figure 5a shows the obvious result: there is a positive
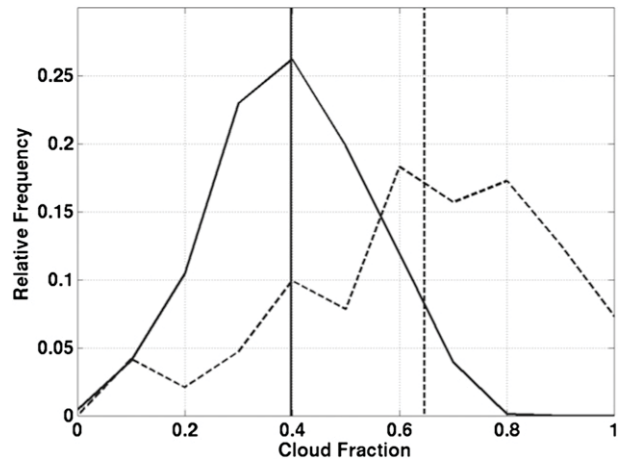

FIG. 4. Distribution of area-averaged cloud fraction for *CloudSat–CALIPSO* (dashed) and ModelE2 (solid). Vertical lines show the distribution means.

difference in cloud amount for the strong-cloud minus weak-cloud subsets. In the observations, the maximum difference occurs in the center of the area-averaging region (Fig. 5a), while in the model it occurs in the upper portion of the averaging region (Fig. 5c). In both cases the positive difference extends into the equatorward side of the transect at altitudes of 7–10 km; however, the extension is deeper and goes much farther equatorward in the model.

Figures 5b and 5d show the difference in ω for the cloud-based subsetting for MERRA and the model. For both cyclone sets, stronger area-average cloud is accompanied by increased upward motion in the frontal tilt region. For MERRA, the increased upward motion is centered on the region of maximum in the composite mean (the contours). In the model, the increase in ω occurs on the poleward edge of the frontal tilt region, implying a stronger poleward tilt in the ω field. Separately, a comparison of Figs. 5c and 5d shows that in the model the maximum differences in cloud and ω occur at different altitudes.

To summarize, along the frontal tilt region, ModelE2 has less cloud and weaker ω than the observations and reanalysis, respectively (Fig. 3), but the modeled cloud and ω covary in a similar qualitative manner to observations/reanalysis (Fig. 5). So, the question is: does the model not produce enough clouds simply because of weak ω, or are there more subtle issues? For instance, the locations of strong cloudiness in observations and strong ω from reanalysis were collocated in the transects, while the model cloud maximum occurs at a higher altitude than that of ω (Fig. 3). Additionally, the differences in the cloud and ω fields for the cloud-based subset are spatially decorrelated in the model, which is
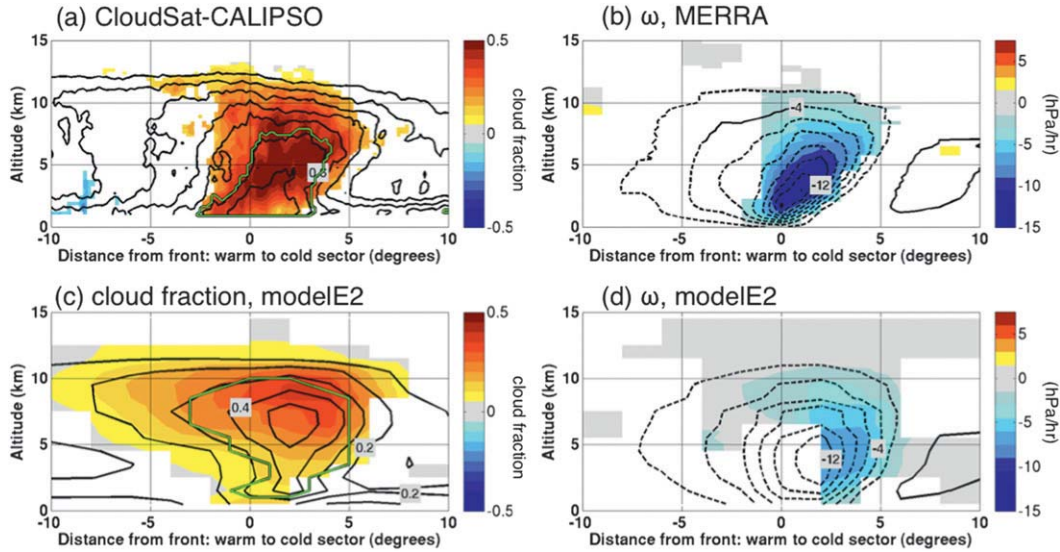
FIG. 5. Cloud-based subset differences (in color), composite means (black contours): area-averaged *CloudSat–CALIPSO* used to subset (a) *CloudSat–CALIPSO* and (b) ω from MERRA and area-averaged ModelE2 cloud used to subset (c) model cloud fraction and (d) ω (hPa h^{-1}). Contour intervals are 0.1 for clouds and 2 hPa h^{-1} for ω; the green contour is the area-averaging region.

not the case in observations (Fig. 5). Therefore, to help understand how the location of strong upward motion affects cloud fraction, we next perform ω-based subsetting using area-averaged ω within the frontal tilt region. If the model cloud differences for ω-based subsets agree with observations/reanalysis, then we know that the order-one cloud physics is behaving correctly.

Figure 6 shows the subset differences of ω and cloud for area averages of ω aloft in the frontal tilt region, defined as 0.5°–5° north of the surface front between 8 and 11 km. Figure 6a shows that in MERRA the maximum subset difference in ω occurs below the area used for averaging. This indicates continuity between the vertical motion aloft and the region below it, which is

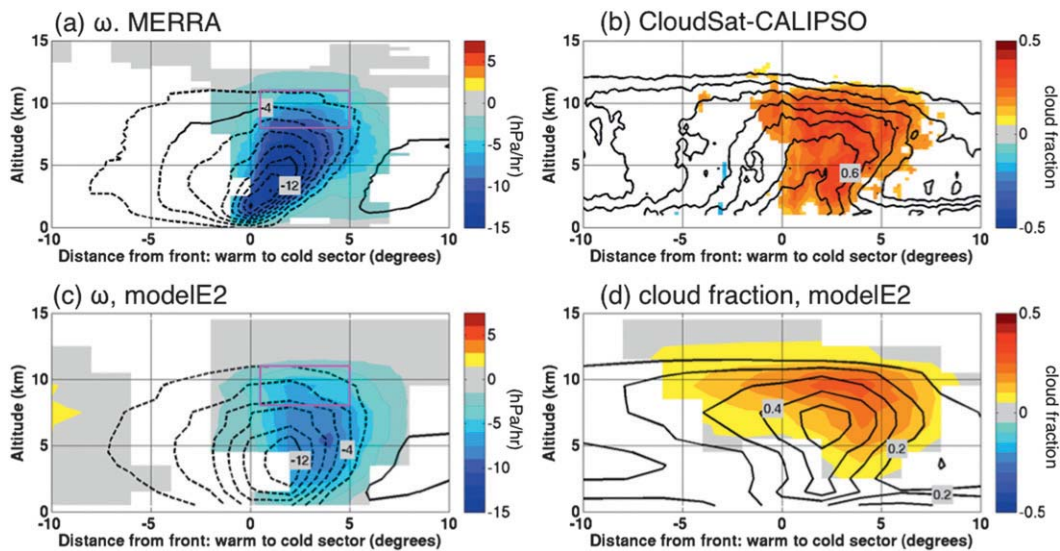FIG. 6. The ω-based subsetting differences using a region between 9 and 11 km (in color), composite means (black contours): area-averaged MERRA ω (hPa h^{-1}) used to subset (a) *CloudSat–CALIPSO* cloud fraction and (b) ω from MERRA and area-averaged ModelE2 ω used to subset model (c) cloud fraction and (d) ω. Contour interval is 0.1 for clouds and 2 hPa h^{-1} for ω. The magenta contour is the area-averaging region.
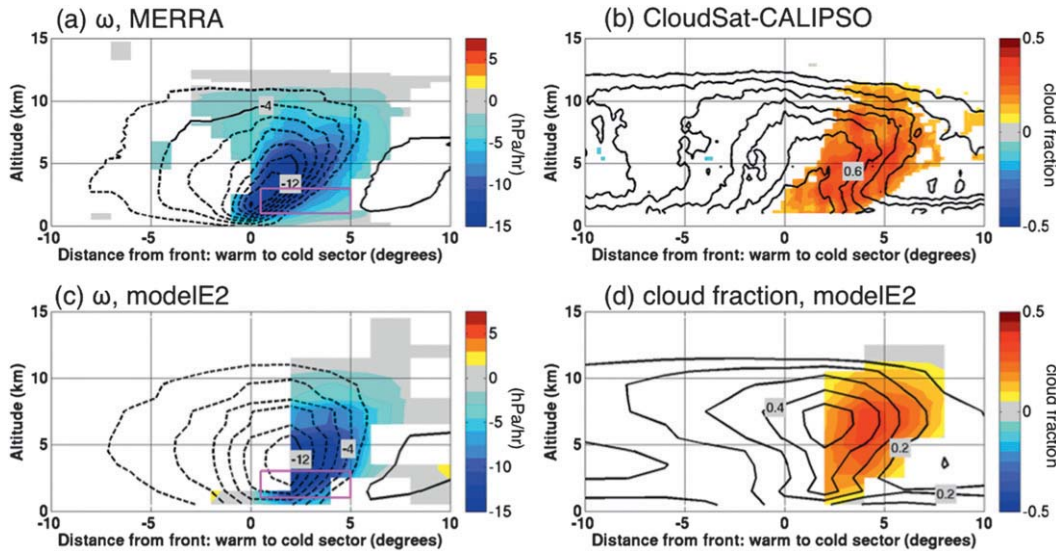
FIG. 7. As in Fig. 6, but using a region between 1 and 3 km.

consistent with the warm conveyor belt (WCB) model that implies a continuous region of vertical motion extending up from the ground (e.g., Carlson 1998, 297–315). Figure 6b shows enhanced cloudiness with stronger upward motion throughout the frontal tilt region for *CloudSat–CALIPSO*.

For the model, Fig. 6c shows an increase in the upward motion throughout the frontal tilt region, but not at the front between 1 and 3 km. Figure 6d shows that the model cloud difference is greatest in the region where the area averaging of ω takes place and below, but not near the surface front. This is consistent with the absence of stronger upward motion at the surface front in Fig. 6c.

Figure 7 shows the ω-based subsetting using an averaging region from 0.5° to 5° north of the surface front between 1 and 3 km. In this case, the maximum difference in the vertical motion occurs within the averaging region in both MERRA and the model (Figs. 7a,c). Figure 7b shows that the observed cloud enhancement occurs at and above the area-averaging region, but only near and poleward of the location of the elevated front (as judged by the peak in mean ω). This differs somewhat from Fig. 6, which shows enhanced cloud associated with stronger upper-level ω also extending equatorward of the elevated front. Note also in Fig. 7a that stronger uplift near the surface front is associated with a bimodal structure of upper-level ω strengthening, with distinct populations of almost upright and very tilted fronts. The model also shows enhanced cloudiness in response to stronger low-level uplift (Fig. 7d), but again this does not extend all the way back to the surface front and the cloud response peaks at higher altitude than the anomalous ω.

For these low-altitude ω subsets, as well as the ω aloft subsets, there is no difference in the geographical location of the cyclones in the strong versus the weak subsets (not shown). This is most likely related to the fact that our analysis only includes cyclones at onset.

The ω-based subsetting suggests that, compared to the observations and reanalysis, 1) vigorous upper-level ω in the GCM is decoupled from ω anomalies at the surface front and 2), although GCM cloudiness is correlated with ω, cloud fraction is less sensitive to stronger uplift near the surface than aloft. The first discrepancy indicates that low-level frontogenesis itself is inadequately represented in the model. The second suggests shortcomings in the cloud parameterization.

To explore the parameterization issues, we consider the relationship between cloud and RH in the model. As discussed in section 2b, GCM stratiform cloud formation depends on gridcell RH. Because of this, the RH differences for the cloud-based and ω-based subsets look very similar to the cloud differences. However, for the subset based on ω aloft, there is a statistically significant increase in low-altitude RH at the warm front (not shown) but no signal in the cloud (Fig. 6c, below 5 km).

Figure 8a shows the across-cyclone correlation between RH and cloud fraction at each latitude/height point in the transect. We define the across-cyclone correlation as follows:

$$\text{RH\_cloud}_{\text{CORR}}(\phi,p) = \frac{\sum_{i=1}^{N} \text{RH}'_i(\phi,p)\,\text{cloud}'_i(\phi,p)}{\sigma(\text{RH}(\phi,p))\sigma(\text{cloud}(\phi,p))},$$

(1)

(a) corr(RH, cloud fraction), modelE2

(b) Convective Heating, modelE2
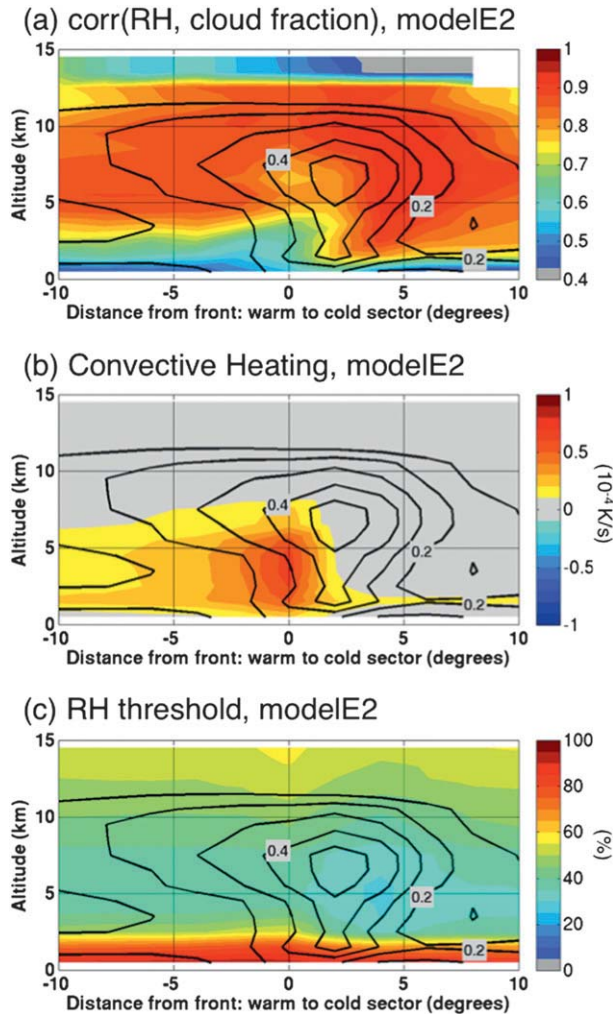

(c) RH threshold, modelE2

FIG. 8. (a) Correlation between RH and cloud fraction across all cyclones in ModelE2 for each latitude/height point in the transect (in color): composite mean cloud fraction (black contours, contour interval 0.1). (b) Convective heating (10^{-4} K s^{-1}) and (c) threshold relative humidity for cloud formation across the model transect.

where cloud is cloud fraction, ϕ is latitude, p is pressure, the primes indicate deviations from the composite mean, i indicates individual transects, N is the total number of cyclone transects, and σ is the standard deviation with respect to the composite mean. Above 5 km in the frontal tilt region, the across-cyclone correlation is strong. The covariability of RH and cloud fraction decreases, though, below ~4 km in the region directly above the surface warm front and behind it and in the lowest 1–2 km throughout the domain. These regions correspond to the areas in which the spatial pattern of the model cloud composite mean differs most from *CloudSat–CALIPSO* (Figs. 3a,c). Two features of the cloud parameterization seem likely to explain this. Figure 8b shows the distribution of convective heating along the frontal transect.
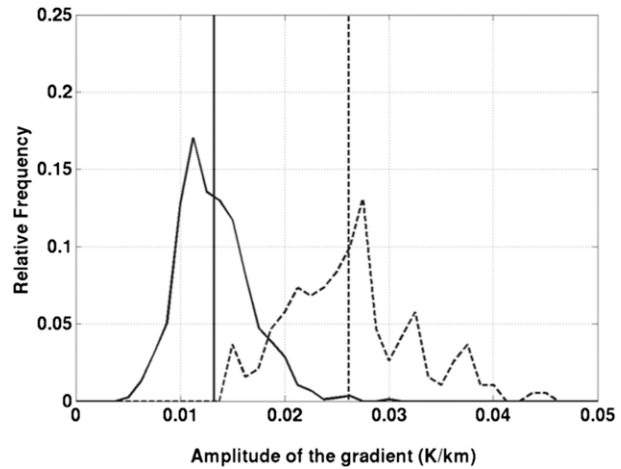

FIG. 9. Distribution of the amplitude of the gradient in θ_{850} (K km^{-1}) averaged along the warm front for MERRA (dashed) and ModelE2 (solid). Vertical lines show the distribution means.

The GCM produces considerable shallow convection in the warm sector behind the surface front and even some deeper upright convection at the location of the surface front. While these are plausible features, the decision to suppress stratiform cloud formation below cloud top in convective regions (which was implemented to improve the model's transition from stratocumulus to trade cumulus in the subtropics) apparently degrades the cloud simulation in extratropical cyclone regions. Likewise, the decision to parameterize threshold RH for cloud formation below 850 hPa as a function of an assumed boundary layer turbulent variance of saturation deficit and not as a function of gridscale uplift (based on subtropical field experiments) may also not be appropriate for the stratus clouds typically found in the extratropics. The distribution of threshold RH across the frontal transect (Fig. 8c) indicates that this decision has made it more difficult to make frontal cloud in the boundary layer than above. Thus, the convective parameterization hinders the expected influence of the RH and ω on the modeled cloud.

b. Subsets based on the warm front temperature gradient

Here we examine cloud and vertical motion subsets based on the amplitude of the meridional gradient of θ at 850 hPa (θ_{850}). Although GCM resolution is too coarse to capture the ageostrophic motions at the warm front that contribute to the vertical motion (e.g., Holton 1992, 175–177), the presence of strong temperature gradients might still be indicative of regions of wind convergence that generates vertical motion. Figure 9 shows the distributions of the warm front gradient, defined here as the average of the gradient at all grid points along the
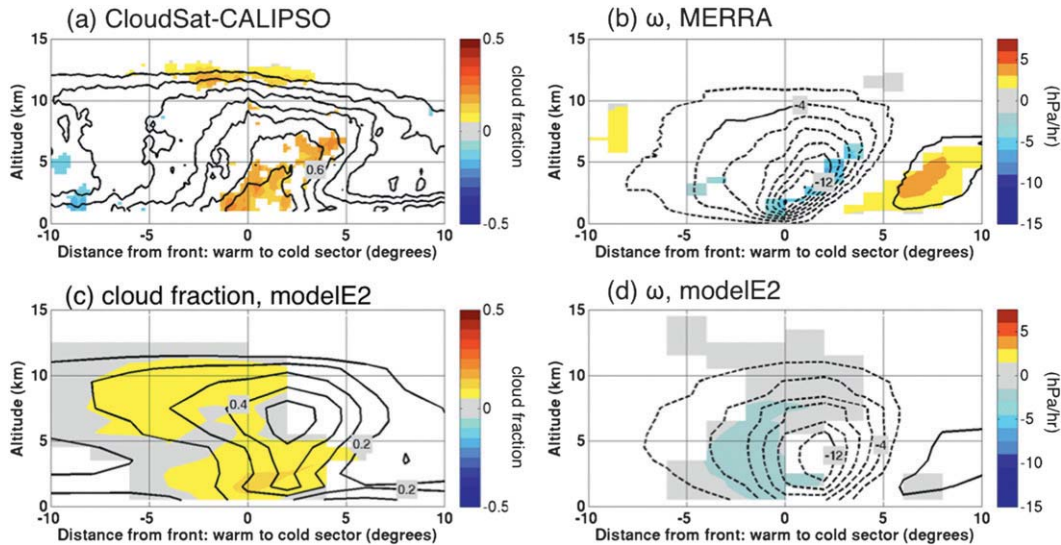
FIG. 10. Temperature gradient-based subsetting differences (in color), composite means (black contours). MERRA warm front used to subset (a) *CloudSat–CALIPSO* cloud fraction and (b) ω from MERRA. ModelE2 warm front temperature gradient used to subset model (c) cloud fraction and (d) ω. Contour interval is 0.1 for clouds and $2\,\mathrm{hPa\,h^{-1}}$ for ω.

detected warm front, from the reanalysis and the model. As expected, the lower-resolution model has much weaker fronts. In a separate test, we analyzed the "bulk" temperature gradient by area averaging θ_{850} over the quadrants northeast and southeast of the cyclone center and differencing the two. For that metric, the model and reanalysis were in close agreement (not shown), indicating that the model generates proper synoptic-scale temperature conditions surrounding the warm front.

Figure 10 shows the results of the temperature-gradient-based subsetting for the clouds and ω transects. For *CloudSat–CALIPSO* cloud fractions, a stronger warm front translates into a weak increase in clouds, mostly within the center of the frontal tilt region (Fig. 10a). The ω difference for the warm front subsets shows a modest increase in upward motion fairly well collocated with the cloud difference (Fig. 10b). The model shows a weak increase in the clouds throughout the warm side of the transect (Fig. 10c). The cloud change at low altitudes within the warm frontal tilt region agrees with the observations, but the differences in the rest of the warm sector are unique to the model. For the ω transect, there is an increase in upward motion on the equatorward side of the warm front (Fig. 10d), which is not consistent with the result for MERRA.

Model strong warm front cyclones are also more concentrated over the longitudes of the oceans' western boundary currents than is true for the reanalysis (Fig. 11). This difference suggests that the model gradients may be more representative of the climatological conditions

than the storm-local circulation, presumably because of the model's coarse resolution. For both observations and model cyclones, the lack of a strong influence of longitudinal location on cyclone cloud properties is most likely related to our use of cyclones at onset only since the western boundary currents are regions of strong cloudiness in the wintertime climatology (Minobe et al. 2010).

Finally, we examined the temperature-gradient-based subsets of the cyclone-local variables wind speed at 850 hPa and precipitable water. For both observations/ reanalysis and the model, the stronger surface gradients correspond to stronger surface winds but no significant difference in PW (not shown). Thus, the low-altitude cloud and vertical motion response appears to be related to the dry circulation rather than moisture availability.

c. Subsets based on cyclone-centered variables

We next consider the cyclone-centered variables wind speed at 850 hPa (wind850) and PW. This analysis is motivated by FW07, who show that the upper-level clouds in cyclones increase with the product of wind850 and PW. We repeat the FW07 analysis for the warm frontal cloud transects and expand on their study by considering the response of the clouds to subsets of each of the variables separately. Our goal is to establish how the clouds along the warm front transect relate to these variables at onset, as well as to test how well the model captures the relationships.
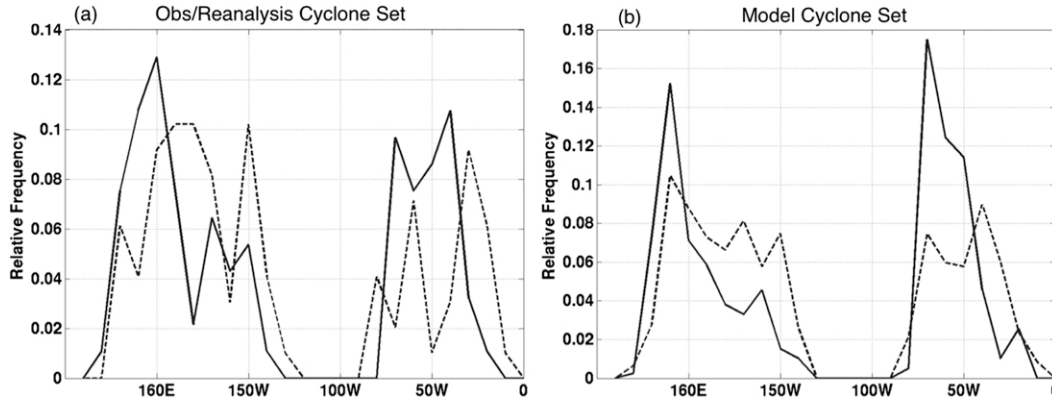
FIG. 11. Distributions of cyclone longitude for subsets with strong warm fronts (solid) and weak warm fronts (dashed), shown for (a) the data/reanalysis cyclone set and (b) the model set.

Figure 12 shows the composite mean for wind850 and PW using all of the cyclones. The MERRA wind850 peaks southeast of the cyclone center (Fig. 12a), which corresponds to the cyclone warm sector. In Fig. 12b, the same region has a latitudinal maximum in PW, which is consistent with the canonical picture of advection of moist air within the cyclone warm sector. For the model, the composite mean for wind850 (Fig. 12c) is very similar
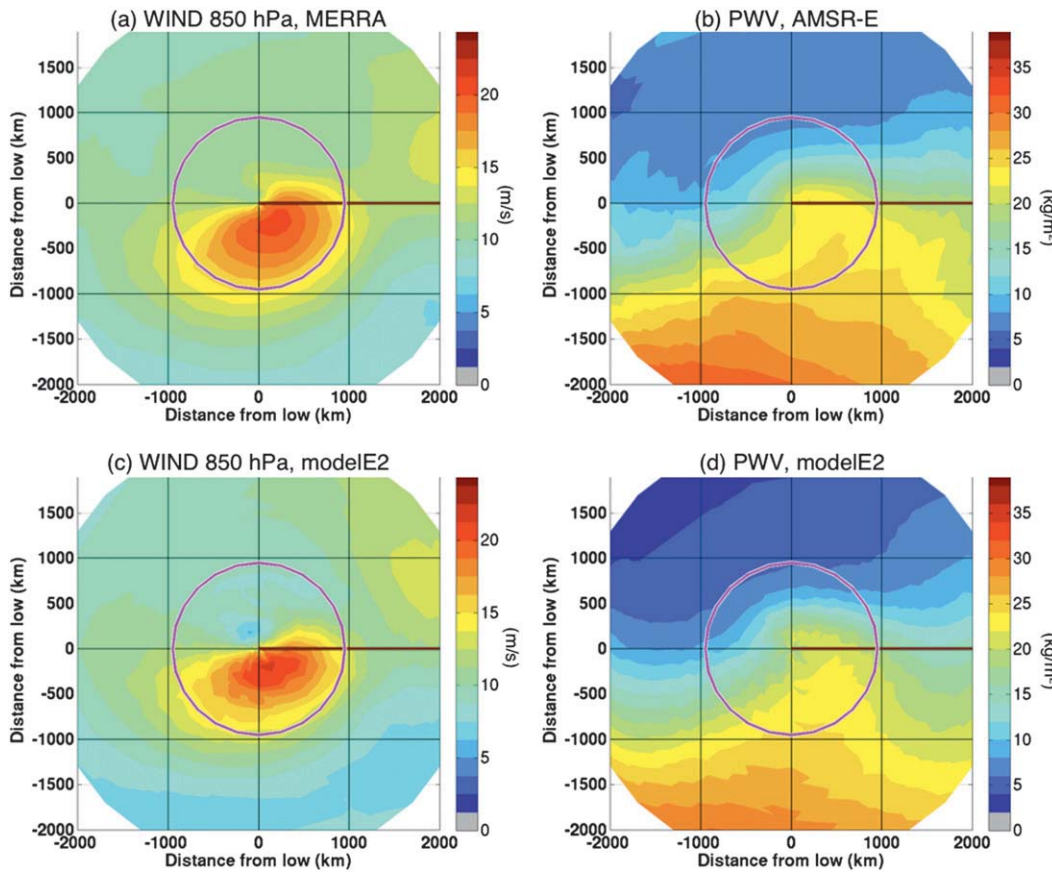

FIG. 12. Composite mean wind850 $(m\,s^{-1})$ and PW $(kg\,m^{-2})$ for all cyclones: (a) MERRA wind850 and (b) AMSR-E PW. ModelE2 (c) wind850 and (d) PW. The bold black line indicates position of the warm front and the magenta circle denotes the area-averaging region.
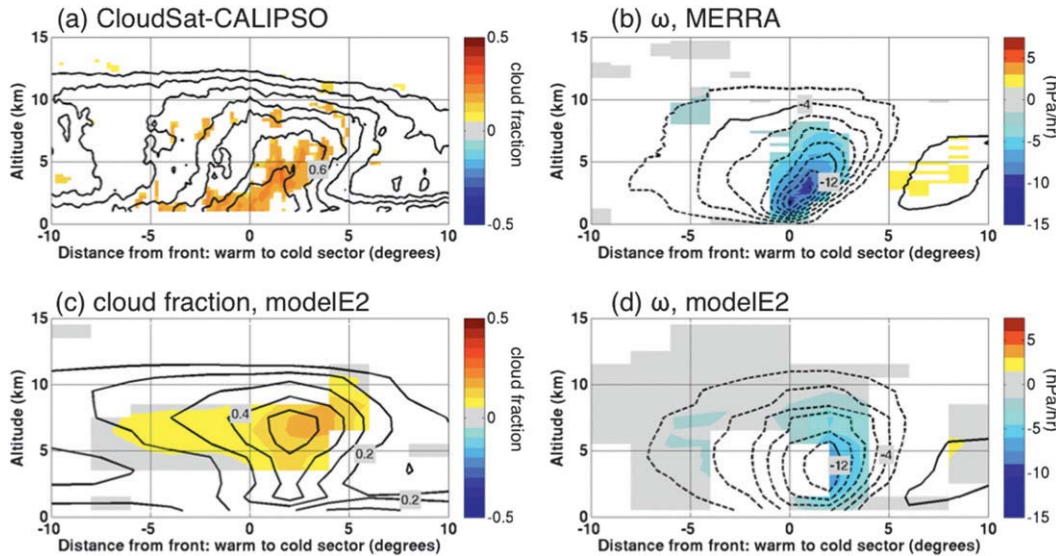
FIG. 13. The wind850-based subsetting differences (in color), composite means (black contours): MERRA wind850 used to subset (a) *CloudSat–CALIPSO* cloud fraction and (b) ω from MERRA. ModelE2 wind850 used to subset model (c) cloud fraction and (d) ω. Contour intervals are 0.1 for clouds and $2\,\mathrm{hPa\,h^{-1}}$ for ω.

to MERRA, though slightly weaker northwest of the low but somewhat stronger southeast of the low. For PW, the model has a well-developed region of high moisture content in the warm sector (Fig. 12d) but is ~10% drier than AMSR-E. To perform the subsetting of the area-averaged wind850 and PW, we use a 1000-km radius and area average around the entire cyclone (the magenta contours in Fig. 12).

First, we consider the wind850-based subsetting for cloud and ω (Fig. 13). The results are similar to those of upper-level ω-based subsetting (Fig. 6): the observed ω and cloud responses to stronger wind850 occur mostly along the warm front at all altitudes, while the model's response is primarily at high altitude and ahead of the front, with little signal near the surface front.

For the PW-based subsetting, observed cyclones with more PW have more cloud in the frontal tilt region, especially at high altitudes, but less cloud behind the front (Fig. 14a). These cloud changes are correlated with changes in ω in the expected sense (Fig. 14b), but stronger upward motion along the front is restricted to the upper troposphere and weak compared to the cloud difference. In other words, frontal clouds are enhanced in a moist environment regardless of whether the frontal dynamics changes.

The model responses to larger PW (Figs. 14c,d) are consistent with the observations at high altitude but, as with other subsets, they exhibit unrealistic behavior near the surface front, with weaker uplift and less cloud in moist conditions. This is another example of the cloud

formation being interfered with by parameterized processes, as discussed in connection with Fig. 8. The more humid subset has more frequent parameterized convection, and the associated convective updrafts might take the place of resolved upward motion, explaining the weaker ω near the surface front.

We also performed subsetting analyses based on the vertical gradient of equivalent potential temperature in the cyclone warm sector and the advection of absolute vorticity at 300 hPa. Neither yields significant differences in the clouds in the observations. Perhaps this is because the first depends more on the cumulus parameterization used for MERRA than any assimilated data, while the second is a third-order quantity and thus noisier than other variables that we use for subsetting. We note though that the model vorticity advection subset had an increase in cloud and upward motion in the frontal tilt region, which suggests that the upper-level forcing does influence the front.

4. Discussion

a. Joint conditional subsetting using PW and wind850

We have seen in the previous section that an increase in precipitable water has more impact on cloud fraction than vertical motion in the frontal tilt, while to some extent the 850-hPa wind increase has more impact on ω than clouds. It is possible that the subsets in each case may be biased, for example, if stronger winds imply drier cyclones. Also, these two variables will jointly affect
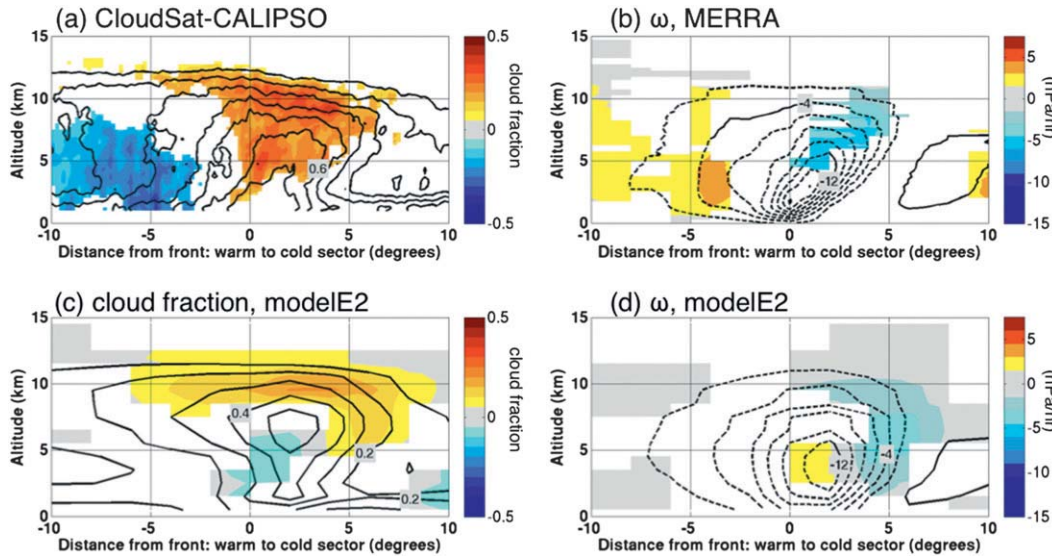
FIG. 14. PW-based subsetting differences (in color), composite means (black contours): AMSR-E PW used to subset (a) *CloudSat–CALIPSO* cloud fraction and (b) ω from MERRA. ModelE2 PW used to subset model (c) cloud fraction and (d) ω. Contour interval is 0.1 for clouds; $2\,hPa\,h^{-1}$ for ω.

clouds and ω; therefore, we explore their relative influence by analyzing joint conditional subsets, as in FW07.

Figure 15 shows the *CloudSat–CALIPSO* composite mean cloud fraction for subsets created by subdividing the cyclones based on both area-averaged MERRA wind850 and AMSR-E PW. We create four subsets, rather than the nine presented in FW07, because of the

limited number of cyclones in our set. Consistent with FW07, the cloud fraction across the warm fronts is greatest at all levels when both wind850 and PW are large (Fig. 15b). From this perspective, the bulk warm conveyor belt (WCB) model of FW07 holds for the cyclones at onset.

Comparing high versus low PW subsets for a given wind850 (Fig. 15a versus Fig. 15c, Fig. 15b versus Fig. 15d)
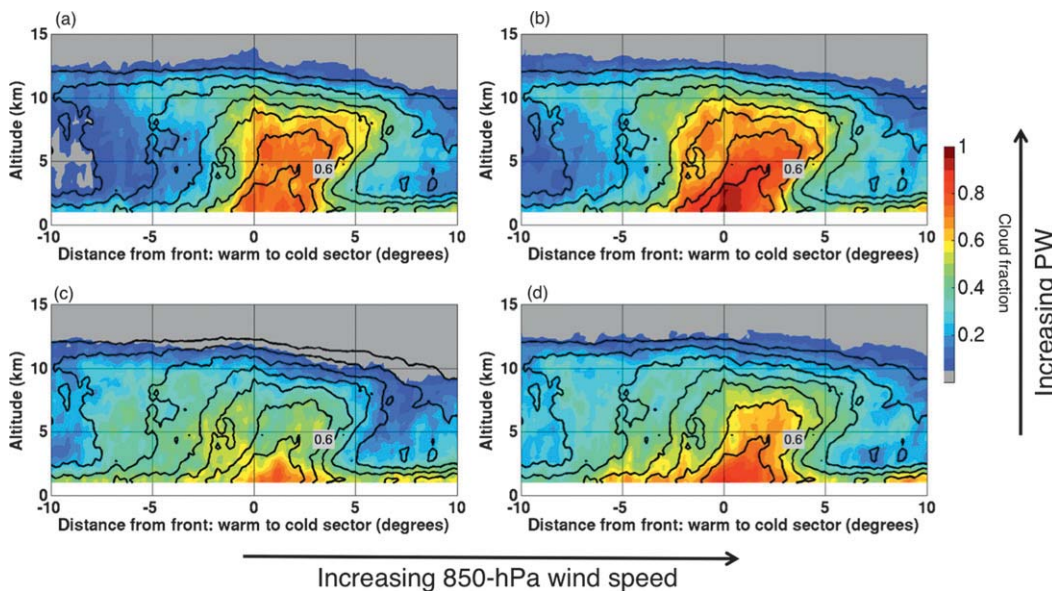

FIG. 15. Subset mean *CloudSat–CALIPSO* cloud fraction using joint conditional subsets based on AMSR-E PW and MERRA wind850 (in color), composite mean for all cyclones (black contours). The subset range for wind850 is 5–14 and 14–22 $m\,s^{-1}$ and for PW 4–17 and 17–50 $kg\,m^{-2}$. The numbers of cyclones per subset are (a) 49, (b) 46, (c) 46, and (d) 50.
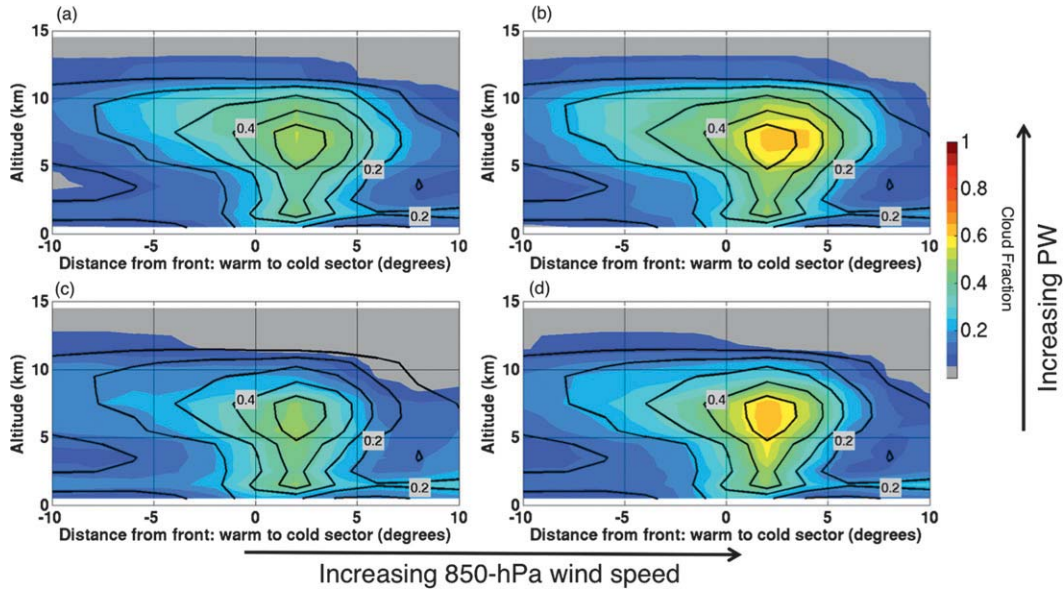
FIG. 16. Subset mean cloud fraction for ModelE2 using joint conditional subsets based on PW and wind850 for the model (in color), composite mean for all cyclones (black contours). The subset range for wind850 is 5–13 and 13–21 m s^{-1} and for PW 2–16 and 16–35 kg m^{-2}. The numbers of cyclones per subset are (a) 268, (b) 164, (c) 162 and (d) 268.

shows that higher PW implies more cloud, but mostly in the upper troposphere. This is qualitatively consistent with the larger ω that is seen at upper levels in Fig. 14b, but our ω signal is much weaker than the cloud response in the frontal region (Fig. 14a). Thus, in the context of the WCB model, if greater high cloud is due to greater moisture flux, it is more due to anomalous moisture than to the vertical motion that transports it. Indeed, the effect of increasing storm strength (Fig. 15b versus Fig. 15a, Fig. 15d versus Fig. 15c) is at best only comparable to the effect of increasing PW. This result differs from that of FW07; it may be related to our focus on cyclones at onset.

Figure 16 shows the corresponding joint conditional subsets of the model cloud fraction for wind850 and PW. Unlike Fig. 15 (but more like FW07), model clouds are fairly insensitive to increasing PW, except for a small increase in high clouds poleward of the front, and are very sensitive to storm strength (at least as defined by wind850). Note, however, two differences between modeled and observed storms: 1) although model wind850 is realistic in the WCB (Fig. 12), peak model ω is only about ¾ as strong as MERRA (Fig. 3); 2) the high PW subset for the model only ranges 16–35 versus 17–50 kg m^{-2} for AMSR-E. Thus, the combination of weak frontal uplift (due to some combination of model resolution and convective suppression) and drier air in the WCB conspires to limit the model sensitivity to moisture changes.

b. Dissecting the cloud response to PW

Here we examine possible reasons for the cloud differences found for the PW-based subsetting. The cyclones with high moisture content tend to occur at lower latitudes than those with low moisture content (not shown). This reflects the meridional gradient in the mean PW. However, subsetting the cyclones based on latitude of the cyclone center (Fig. 17) shows a weak increase in cloudiness in the frontal region in both data and model. This is consistent with the FW07 finding that cyclone-average RH is independent of SST, and it means that the increase in cloud for PW-based subsetting is not caused by the latitude difference alone. Climatological PW conditions also have a seasonal bias; however, the PW-based subsets do not have seasonal dependence (not shown). Thus, the increased frontal cloudiness in the strong PW subset is caused by cyclone local circulation differences.

Next, we examine the decrease in observed midlevel cloudiness 5°–10° equatorward of the surface front for the PW-based subsetting (Fig. 14a). One explanation for this difference is based on differences in the cyclone orientation relative to the transects, which we can examine with the mean SLP contours for the high and low subsets (Figs. 18a,b). For high PW, the composite mean SLP resembles a weak cutoff low with a southwest to northeast tilt. For low PW, the SLP minimum is deeper and the circulation south of the center has less of a tilt.
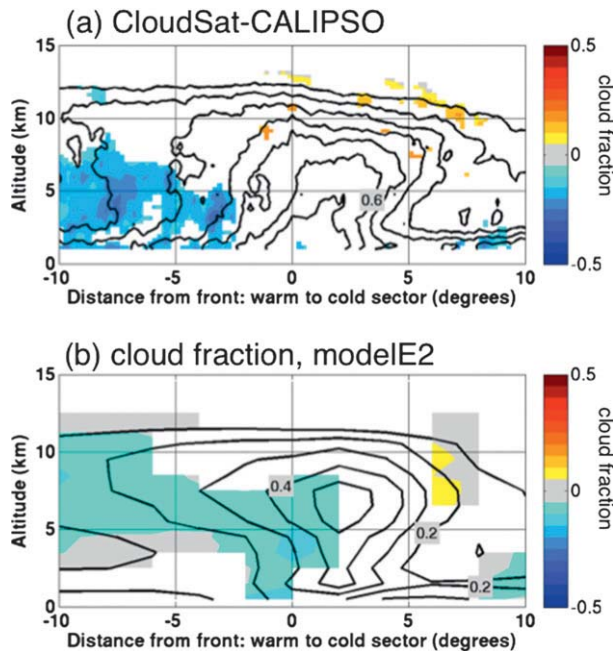
FIG. 17. Latitude-based subsetting differences (low-latitude minus high-latitude cyclones) (in color), composite means (black contours). (a) Reanalysis cyclone latitude used to subset *CloudSat–CALIPSO* cloud fraction and (b) model cyclone latitude used to subset model cloud fraction. Contour interval is 0.1 for clouds and $2\,hPa\,h^{-1}$ for ω.

The 500-hPa ω corroborates these differences in orientation (Figs. 18a,b). Furthermore, RH transects (Figs. 18c,d) show that the region of negative cloud difference corresponds to a RH minimum between 2 and 6 km in the high PW case. A comparison of the temperature profiles along the transects (Figs. 18c,d) suggest that the high PW cases have much warmer air aloft, which keeps the RH low. The cause of this will be the subject of future research. Here we simply want to show that the cloud differences in this region (5°–10° equatorward of the front) are consistent with both the dynamical and thermodynamical differences in the PW subsets. Also, south of the front, circulation differences between the low- and high-latitude cyclones are similar to that of low versus high PW (not shown). This reinforces the argument that the difference in cyclone orientation explains the cloud response since the latitude-based subsets have a similar difference in cloud fraction 5°–10° equatorward of the front (Fig. 17a).

5. Conclusions

In this study warm frontal clouds of extratropical cyclones are examined, focusing on the onset phase of the storm life cycles. We create a dataset of extratropical cyclones coincident with *CloudSat–CALIPSO* transects

for comparison with those in the GISS ModelE2 GCM. Subsets of the cloud field were defined conditionally, based on cyclone-local variables obtained from reanalysis, observations, and the model. Conditional subsetting confirms a strong relationship between observed frontal cloudiness and ω at all altitudes. The cyclone-averaged 850-hPa wind speed and, to a lesser extent, the temperature gradient at the front impact both clouds and ω within the frontal tilt region, especially at low levels. On the other hand, precipitable water (PW) has no impact on ω in the frontal region except at high altitude, while it has a strong impact on the cloudiness, especially above 3 km.

ModelE2 cyclones do not produce enough cloud, especially at low altitudes. Consistent with this, the model ω field is too weak and does not have enough poleward tilt with height. Additionally, the model warm front temperature gradients are too weak, although the cyclone-centered composite mean wind speed at 850 hPa looks similar for the model and reanalysis. The same is true for PW, except that the model has slightly less moisture at the warm front. The fact that the cyclone transects of cloud differ for the model and observations/reanalysis, while the cyclone-centered composites of environmental state agree can be explained by the subsetting analysis, which shows that the model's sensitivity to these variables is too weak.

We summarize the aspects of agreement and disagreement between the observations/reanalysis and model below.

Agreement

- Cloud fraction on the poleward edge of the frontal tilt region increases with the low-level vertical motion.
- Upward motion in the frontal region increases with area-averaged 850-hPa winds.
- Cloud fraction above 7 km in the frontal region increases with area-averaged PW.

Disagreement

- Cloud fraction and ω near the surface front in the model is decoupled from upper-level cloud fraction and ω.
- Model cloud between 3 and 7 km varies too strongly with wind850, while cloud below 3 km does not vary enough.
- Model cloud between 3 and 7 km varies with PW in an opposite manner to that in observations.

The most striking result is the disconnect between the model's high-altitude and low-altitude clouds and ω in the warm frontal region. It may help explain why the composite mean cloud field appears top heavy compared to the observations (Fig. 3): high-altitude cloud
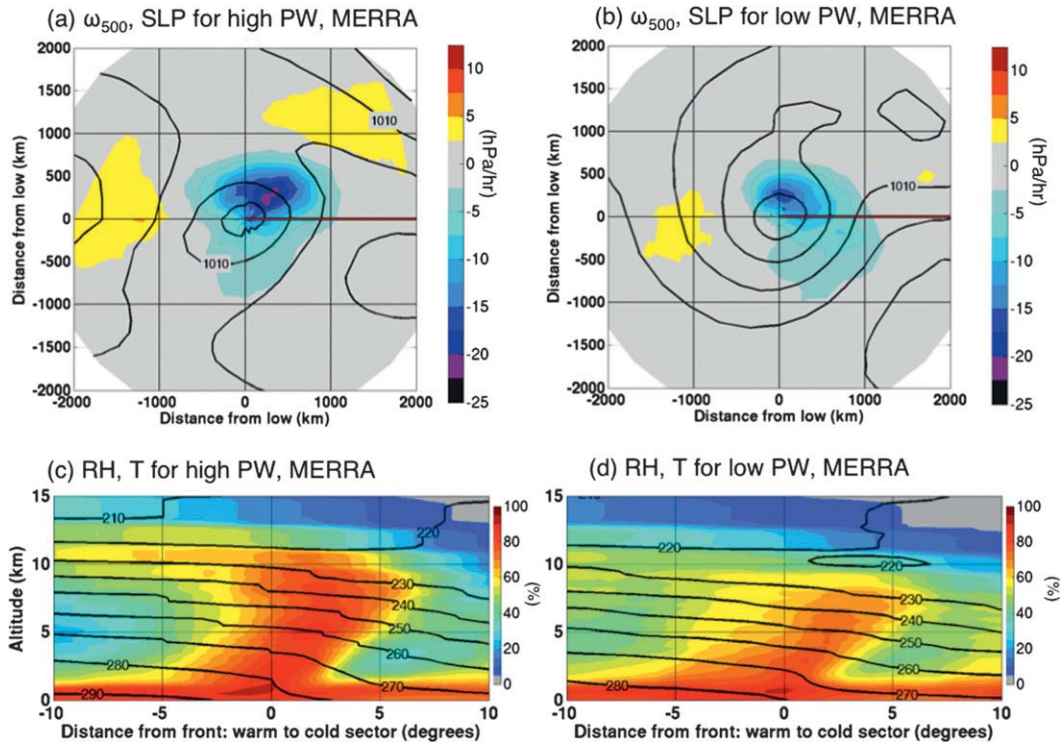
FIG. 18. Subset mean for MERRA (a),(b) SLP (hPa, contours) and ω_{500} (hPa h^{-1}, color) and (c),(d) temperature (K, contours) and RH (%, color) for (a),(c) high PW and (b),(d) low PW.

formation is not occurring in step with low-altitude clouds. The issue for low-altitude cloud is more complicated because it coincides with a region in which the cloud, convection, and planetary boundary layer (PBL) schemes are all active. Regions in which clouds are poorly correlated with RH coincide with the occurrence of parameterized moist convection that suppresses stratiform cloud formation.

These results suggest that parameterization choices appropriate for subtropical convective PBLs do not work well in extratropical frontal regions containing stratus. Recent changes to the cumulus parameterization to suppress convection penetration and increase convective moistening in the tropics (Del Genio et al. 2012) may also be beneficial for the extratropics. The absence of a parameterization of slantwise convection may also play a role in the frontal region (Naud et al. 2010). A separate possibility is that recent changes to the GISS PBL scheme (Yao and Cheng 2012) may improve the availability of moisture to the WCB. Our subsetting analysis also revealed that some of the issues in the model relate to resolution. Therefore, we plan to analyze a version of ModelE2 with a finer horizontal and vertical resolution.

Finally, we have demonstrated how conditional subsetting can 1) isolate specific model problems that may not be perceptible in large-scale averages and 2) provide clues as to where the model physics should be improved. This tool also helps to test the model response to changes even when the mean state does not match observations. As such, it allows an evaluation of the model's ability to reproduce climate variability and not just the present mean climate.

TABLE A1. Correlation of area average clouds vs averaging region in percentiles.

	Lower bound of the top percentile				
	90th	85th	80th	75th	70th
Cloud fraction cutoff in the composite mean	36%	30.4%	27%	24%	23%
Percentile	Correlation with average				
90th	1	0.97	0.94	0.88	0.82
85th		1	0.95	0.89	0.84
80th			1	0.95	0.91
75th				1	0.97
70th					1

TABLE A2. Correlations of area average wind speed at 850 hPa and PW vs averaging region radius.

Variable being averaged	Radius (km)	Radius of the averaging circle centered on the cyclone			
		500 km	1000 km	1500 km	2000 km
wind850	500	1	0.79	0.59	0.46
	1000		1	0.91	0.79
	1500			1	0.96
	2000				1
PW	1000	0.96	1	0.98	0.95
wind850 × PW	1000	0.76	1	0.89	0.79

APPENDIX

Sensitivity to Area-Averaging Region

Here, we test the sensitivity of the cloud area-averaging results to the size of the area used in section 3a. To do this, we repeat the averaging using cutoff percentiles of 90, 80, 75, and 70 and then calculate the correlation between the sets of area averages for the different regions (Table A1). The set using the 85% cutoff has a correlation greater than 0.8 with each of the sets using different cutoffs. This suggests that subsetting based on these different area averages will include many of the same cyclones.

Next, we test the robustness of the wind850 and precipitable water results by calculating the correlation between the area averages of the same variable for different size regions, starting with wind850 in section 3c. For areas whose radii are greater than 1000 km, the averages have strong correlations, while the set of averages for a 500-km radius has weaker correlation with the larger area sets (Table A2). However, since our study focuses on cyclones at onset when they are smaller, it is not clear which radius is most relevant. FW07 used a radius of 2000 km, but their study included cyclones at all stages in a storm's life cycle. Therefore, we compromise and use a radius of 1000 km.

In the case of PW, the sensitivity to the averaging area is much simpler. The correlations between different averaging regions are always larger than 0.8 (Table A2). In addition, the correlation between the averages using a full circle and those using only the region southeast of the cyclone center are strong (not shown). Therefore, all of our analysis of PW uses the full circular area centered on the cyclones with radius 1000 km.

REFERENCES

Bauer, M., and A. D. Del Genio, 2006: Composite analysis of winter cyclones in a GCM: Influence on climatological humidity. *J. Climate,* **19,** 1652–1672.

Bengtsson, L., K. I. Hodges, and N. Keenlyside, 2009: Will extratropical storms intensify in a warmer climate? *J. Climate,* **22,** 2276–2301.

Bodas-Salcedo, A., K. D. Williams, P. R. Field, and A. P. Lock, 2012: The surface downwelling solar radiation surplus over the Southern Ocean in the Met Office model: The role of midlatitude cyclone clouds. *J. Climate,* **25,** 7467–7486.

Bony, S., J.-L. Dufresne, H. Le Treut, J.-J. Morcrette, and C. Senior, 2004: On dynamic and thermodynamic components of cloud changes. *Climate Dyn.,* **22,** 71–86, doi:10.1007/s00382-003-0369-6.

Booth, J. F., S. Wang, and L. Polvani, 2013: Midlatitude storms in a moister world: Lessons from idealized baroclinic life cycle experiments. *Climate Dyn.,* doi:10.1007/s00382-012-1472-3, in press.

Carlson, T. N., 1998: *Mid-Latitude Weather Systems.* University of Chicago Press, 507 pp.

Catto, J. L., L. C. Shaffrey, and K. I. Hodges, 2010: Can climate models capture the structure of extratropical cyclones? *J. Climate,* **23,** 1621–1635.

——, C. Jakob, G. Berry, and N. Nicholls, 2012: Relating global precipitation to atmospheric fronts. *Geophys. Res. Lett.,* **39,** L10805, doi:10.1029/2012GL051736.

Chang, E. K. M., and S. W. Song, 2006: The seasonal cycles in the distribution of precipitation around cyclones in the western North Pacific and Atlantic. *J. Atmos. Sci.,* **63,** 815–830.

Del Genio, A. D., M.-S. Yao, W. Kovari, and K. K.-W. Lo, 1996: A prognostic cloud water parameterization for global climate models. *J. Climate,* **9,** 270–304.

——, Y.-H. Chen, D. Kim, and M.-S. Yao, 2012: The MJO transition from shallow to deep convection in *CloudSat/CALIPSO* data and GISS GCM simulations. *J. Climate,* **25,** 3755–3770.

Field, P. R., and R. Wood, 2007: Precipitation and cloud structure in midlatitude clouds. *J. Climate,* **20,** 233–254; Corrigendum, **20,** 5208–5210.

——, A. Gettelman, R. B. Neale, R. Wood, P. J. Rasch, and H. Morrison, 2008: Midlatitude cyclone compositing to constrain climate model behavior using satellite observations. *J. Climate,* **21,** 5887–5903.

——, A. Bodas-Salcedo, and M. E. Brooks, 2011: Using model analysis and satellite data to assess cloud and precipitation in

midlatitude cyclones. *Quart. J. Roy. Meteor. Soc.,* **137,** 1501–1515.

Haynes, J. M., C. Jakob, W. B. Rossow, G. Tselioudis, and J. Brown, 2011: Major characteristics of Southern Ocean cloud regimes and their effects on the energy budget. *J. Climate,* **24,** 5061–5080.

Held, I. M., and B. J. Soden, 2006: Robust responses of the hydrological cycle to global warming. *J. Climate,* **19,** 5686–5699.

Hewson, T. D., 1998: Objective fronts. *Meteor. Appl.,* **5,** 37–65.

Hodges, K. I., R. W. Lee, and L. Bengtsson, 2011: A comparison of extratropical cyclones in recent reanalyses ERA-Interim, NASA MERRA, NCEP CFSR, and JRA-25. *J. Climate,* **24,** 4888–4906.

Holton, J. R., 1992: *An Introduction to Dynamic Meteorology.* 3rd ed. Academic Press, 511 pp.

Kärcher, B., and U. Lohmann, 2002: A parameterization of cirrus cloud formation: Homogeneous freezing of supercooled aerosols. *J. Geophys. Res.,* **107,** 4010, doi:10.1029/2001JD000470.

Kawanishi, T., and Coauthors, 2003: The Advanced Microwave Scanning Radiometer for the Earth Observing System (AMSR-E), NASDA's contribution to the EOS for global energy and water cycle studies. *IEEE Trans. Geosci. Remote Sens.,* **41,** 184–194.

Lau, N. C., and M. W. Crane, 1995: A satellite view of the synoptic-scale organization of cloud properties in midlatitude and tropical circulation systems. *Mon. Wea. Rev.,* **123,** 1984–2006.

Mace, G. G., Q. Xhang, M. Vaughan, R. Marchand, G. Stephens, C. Trepte, and D. Winker, 2009: A description of hydrometeor later occurrence statistics derived from the first year of merged Cloudsat and CALIPSO data. *J. Geophys. Res.,* **114,** D00A26, doi:10.1029/2007JD009755.

Marchand, R., G. G. Mace, T. Ackerman, and G. Stephens, 2008: Hydrometeor detection using *Cloudsat*—An Earth-orbiting 94-GHz cloud radar. *J. Atmos. Oceanic Technol.,* **25,** 519–533.

Minobe, S., M. Masato, A. Kuwano-Yoshida, H. Tokinaga, and S.-P. Xie, 2010: Atmospheric response to the Gulf Stream: Seasonal variations. *J. Climate,* **23,** 3699–3719.

Naud, C. M., A. D. Del Genio, and M. Bauer, 2006: Observational constraints on the cloud thermodynamic phase in midlatitude storms. *J. Climate,* **19,** 5273–5288.

——, ——, ——, and W. Kovari, 2010: Cloud vertical distribution across warm and cold fronts in *CloudSat–CALIPSO* data and a general circulation model. *J. Climate,* **23,** 3397–3415.

——, D. J. Posselt, and S. C. van den Heever, 2012: Observational analysis of cloud and precipitation in midlatitude cyclones: Northern versus Southern Hemisphere warm fronts. *J. Climate,* **25,** 5135–5151.

Neu, U., and Coauthors, 2013: IMILAST—A community effort to intercompare extratropical cyclone detection and tracking algorithms: Assessing method-related uncertainties. *Bull. Amer. Meteor. Soc.,* **94,** 529–547.

Pinto, J. G., S. Zacharias, A. H. Fink, G. C. Leckebusch, and U. Ulbrich, 2009: Factors contributing to the development of extreme North Atlantic cyclones and their relationship with the NAO. *Climate Dyn.,* **32,** 711–737.

Rayner, N. A., E. B. Horton, D. E. Parker, C. K. Folland, and R. B. Hackett, 1996: Version 2.2 of the global sea-ice and sea surface temperature dataset, 1903-94. Met Office Hadley Centre Climate Research Tech. Note 74, 50 pp.

Rienecker, M. M., and Coauthors, 2011: MERRA: NASA's Modern-Era Retrospective Analysis for Research and Applications. *J. Climate,* **24,** 3624–3648.

Rudeva, I., and S. K. Gulev, 2011: Composite analysis of North Atlantic extratropical cyclones in NCEP–NCAR reanalysis data. *Mon. Wea. Rev.,* **139,** 1419–1446.

Siebesma, A. P., and Coauthors, 2003: A large eddy simulation intercomparison study of shallow cumulus convection. *J. Atmos. Sci.,* **60,** 1201–1219.

Simmons, A. J., S. M. Uppala, D. Dee, and S. Kobayashi, 2007: ERA-Interim: New ECMWF reanalysis product from 1989 onwards. *ECMWF Newsletter,* No. 110, ECMWF, Reading, United Kingdom, 25–35.

Stephens, G. L., and Coauthors, 2002: The CloudSat mission and the A-Train: A new dimension to space-based observations of clouds and precipitation. *Bull. Amer. Meteor. Soc.,* **83,** 1771–1790.

——, and Coauthors, 2010: Dreary state of precipitation in global models. *J. Geophys. Res.,* **115,** D24211, doi:10.1029/2010JD014532.

Stoelinga, M. T., 1996: A potential vorticity-based study on the role of diabatic heating and friction in a numerically simulated baroclinic cyclone. *Mon. Wea. Rev.,* **124,** 849–874.

Trenberth, K. E., and J. T. Fasullo, 2010: Simulation for present-day and twenty-first-century energy budgets of the southern oceans. *J. Climate,* **23,** 440–454.

Tselioudis, G., and W. B. Rossow, 2006: Climate feedback implied by observed radiation and precipitation changes with midlatitude storm strength and frequency. *Geosphy. Res. Lett.,* **33,** L02704, doi:10.1029/2005GL024513.

——, Y.-C. Zhang, and W. B. Rossow, 2000: Cloud and radiation variations associated with Northern Hemisphere low and high sea level pressure regimes. *J. Climate,* **13,** 312–327.

Wentz, F., and T. Meissner, 2004: AMSR-E/Aqua L2B global swath ocean products derived from Wentz algorithm version 2, 2006-2009. National Snow and Ice Data Center, Boulder, CO, digital media. [Available online at http://nsidc.org/data/ae_ocean.html.]

Winker, D. M., M. A. Vaughan, A. H. Omar, Y. Hu, K. A. Powell, Z. Liu, W. H. Hunt, and S. A. Young, 2009: Overview of the *CALIPSO* mission and CALIOP data processing algorithms. *J. Atmos. Oceanic Technol.,* **26,** 2310–2323.

Yao, M.-S., and Y. Cheng, 2012: Cloud simulations in response to turbulence parameterizations in the GISS Model E GCM. *J. Climate,* **25,** 4963–4974.